IEEE Photonics Journal
An IEEE Photonics Society Publication

Open Access

Perfect Chirped Echelle Grating Wavelength Multiplexor: Design and Optimization

Volume 5, Number 2, April 2013

Richard J. Lycett
Dominic F. G. Gallagher, Member, IEEE
Vincent J. Brulis

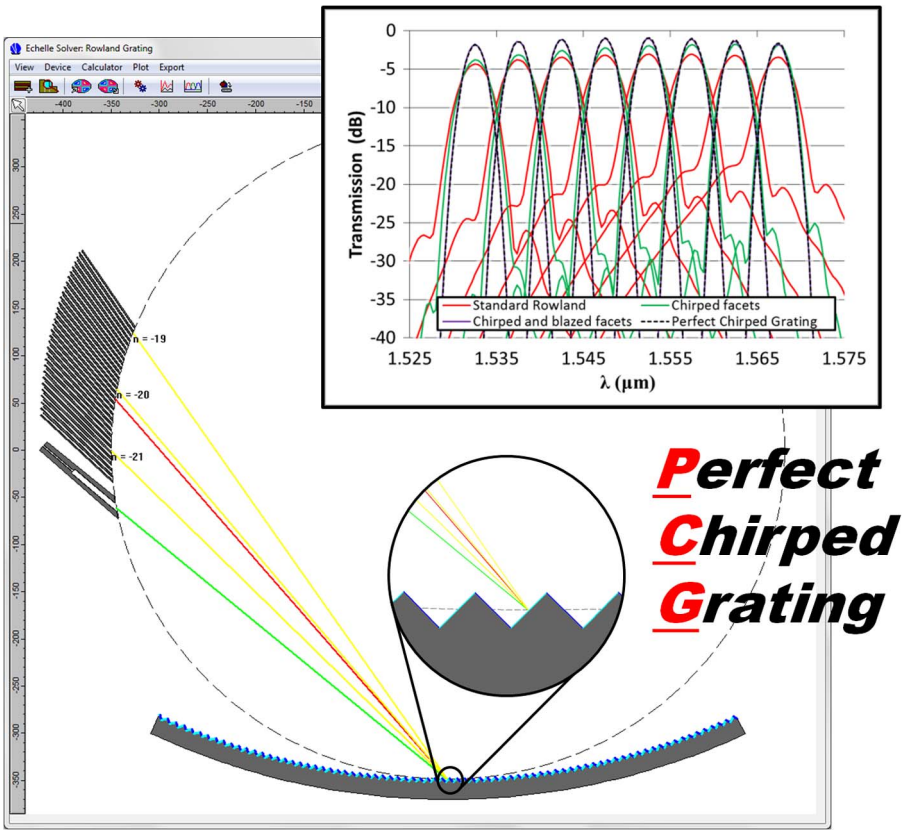

DOI: 10.1109/JPHOT.2013.2251874
1943-0655/$31.00 ©2013 IEEE

IEEE photonics SOCIETY

IEEE

Perfect Chirped Echelle Grating Wavelength Multiplexor: Design and Optimization

Richard J. Lycett, Dominic F. G. Gallagher, *Member, IEEE*, and Vincent J. Brulis

Photon Design, Oxford OX4 1TW, U.K.

DOI: 10.1109/JPHOT.2013.2251874
1943-0655/$31.00 ©2013 IEEE

Manuscript received January 24, 2013; revised February 27, 2013; accepted February 28, 2013. Date of publication March 13, 2013; date of current version March 19, 2013. Corresponding author: R. J. Lycett (e-mail: rlycett@photond.com).

Abstract: A new method for designing an echelle-type diffraction grating for wavelength division multiplexing (WDM), which is tuned to a single stigmatic point, is introduced. The new grating is defined by the mode and wavelength of operation in a slab waveguide, the position of the waveguides, the order of diffraction, and an arbitrary path, which is called the grating line, upon which individual facets are positioned, blazed, and curved via the outlined algorithm. A systematic design process for echelle gratings (EGs) is presented, covering all the key aspects of this device. A series of rules to improve the performance of any EG WDM device is outlined. A simulated comparison between this device, a standard Rowland grating, and a two stigmatic point grating, was undertaken with the new design performing better and comparably in each case, respectively.

Index Terms: Gratings, modeling, theory and design, waveguide devices.

1. Introduction

Wavelength division multiplexing (WDM) is widely used in the telecommunications industry to expand the bandwidth available in the current fiber optic infrastructure. Expanding the bandwidth requires more refined, cheap, and reproducible wavelength splitting. One solution to this is using integrated planar lightwave circuits. WDM in such devices comes in a few flavors, including arrayed waveguide gratings (AWGs) [1]–[3], echelle gratings (EGs) [4]–[6], and Mach–Zehnder interferometers [7], [8]. In this paper, we introduce a novel way of defining an EG based upon a Rowland circle (RC) geometry that has a theoretically low insertion loss with low noise, which is better than a standard Rowland grating and shows comparable performance with a two stigmatic (aka anastigmatic) point grating [9], [10]. We also present a systematic methodology for the optimization of EGs in general, including layout compromises and facet design.

Shown in Fig. 1 is a standard Rowland mounting [11] as would be etched into a slab waveguide. The grating facets of a flat diffraction grating are projected onto a circular section whose radius is equal to the diameter of a circle upon which the input waveguide (InWG) and output waveguides (OutWGs) are mounted, which is called the RC. The circular section and the RC meet at a point in the center of the grating. This concave grating provides focusing for an input diverging beam such that each of the orders is focused to a different point around the RC at the angle determined by the standard diffraction equation

$$d(\sin(\theta_{\mathrm{IN}}) + \sin(\theta_m)) = \frac{m\lambda}{n_{\mathrm{eff}}} \tag{1}$$

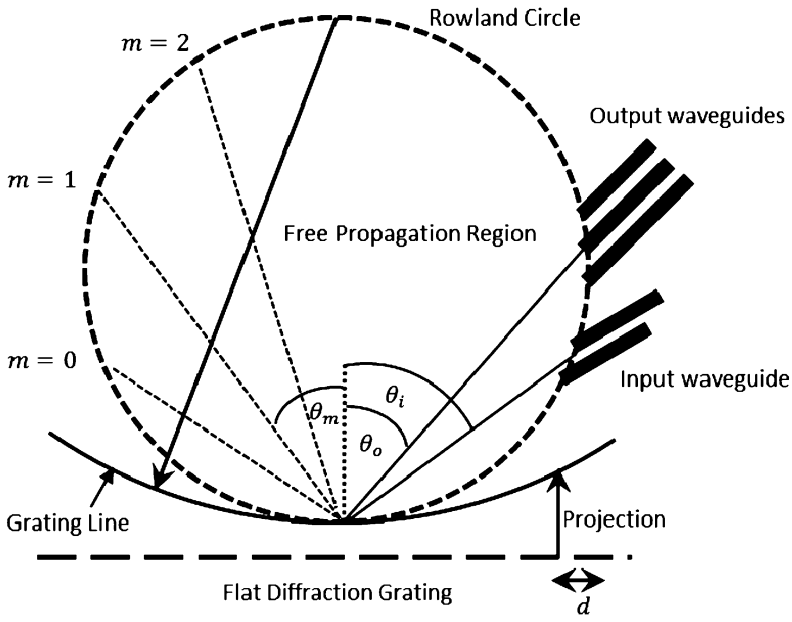

Fig. 1. Shows a typical Rowland mounting with waveguides as would be etched into a slab waveguide. Note that, in this and all following images, the black region denotes the etched regions between waveguides.

where d is the period of the grating, θ_{IN} is the angle of incidence, θ_m is the angle of diffraction associated with an order, m is the order of diffraction, λ is the wavelength in free space, and n_{eff} is the effective refractive index of the mode in the slab waveguide at that wavelength.

The grating is used in a reflective geometry, and a tilt or a blaze to the facets can be applied to channel intensity into the desired order. Light is injected from an etched InWG into an unetched slab region, which is called the free propagation region (FPR); it is then reflected, diffracted, and focused by the grating to the position of the etched OutWG array where it is coupled out. The position of the resultant image on the OutWG array varies with the wavelength. If the radius of curvature is small compared to the length of the grating, then the phase difference between light reflecting from adjacent facets on the curved grating can vary with position and the phase coherence and the performance of the device can be impaired.

We propose a method whereby the focusing effect of the Rowland mounting can be matched with the perfect phase behavior between neighboring facets. A series of algorithms has been developed to space the facets of the grating such that the phase behavior at a specific wavelength is maintained. Additionally, the tilt and curvature of each individual facet is determined to maximize the phase coherence at a specific point. By construction, the resulting grating has one perfect stigmatic point at a specific wavelength independent of initial choice of the grating line and the position of light source and receiver.

2. Design

The definition of each grating facet falls into three distinct steps as follows: A) the position of the facet center and length; B) the facet blaze; and C) the facet curvature. These are uniquely defined by i) a grating line, i.e., the nominal line upon which the facets are placed, ii) a wavelength of operation, iii) the InWG and OutWG array positions, and iv) the order of the grating. All grating optimization is done using a single mode in the FPR. For simplicity, we shall refer to the resulting design based upon a grating line defined along the standard Rowland mount as the "*perfect chirped grating*" (PCG), although it involves more than just the chirp. It is worth noting that the method outlined below will work with any grating line and is not limited to RC devices.

2.1. Defining the Facet Center and Spacing

The algorithm to define the facets is given the following parameters: the angular position of the InWG and the center of the OutWG array relative to the grating normal, θ_i and θ_o, respectively; a chosen mode of operation m; the epitaxy and mode of operation in the slab waveguide, defining the effective index of the slab n_{eff}; the length of the requested grating L; the wavelength of operation λ_c; and the Rowland radius R. The grating line is taken to be along the Rowland mount, which is a circular section that meets the RC at the center of the grating and has radius $2R$ (see Fig. 1). We define, at this point, $\lambda_{\text{FPR}} = \lambda_c/n_{\text{eff}}$, which is the wavelength of the light in the chosen slab waveguide mode of operation.

Each facet along a grating line should be positioned along the grating line such that:

1) the facet center of facet j lies on the grating line, with $j = 0$ indicating the central facet of the grating;
2) the path l_j from the InWG center, at r_{in}, to the facet r_j to the OutWG array center r_{out} should differ from its neighbor by an integer number of wavelengths in the slab waveguide determined by the order of the grating, i.e., by $m\lambda_{\text{FPR}}$;
3) each facet will be terminated at a point along a line that is perpendicular to the facet face and passes through the grating line at a point associated with destructive interference with the light reflected from the facet center, i.e., with a path difference relative to the center of $\pm m\lambda_{\text{FPR}}/2$.

Obeying these three rules defines a series of facets whose position and length are determined by constructive interference between the points on the facet centers and destructive interference conditions between the center and the point at which the facet is terminated on either end, effectively defining the length. All these cardinal points can be found by fitting path lengths l_j and $l_{j\pm0.5}$.

The algorithm used is based upon the following outline.

1) The path length l_0 is calculated via the central facet at r_0.
2) A path length is calculated to the most left hand end, i.e., l_l, of the grating. This is positioned $-L/2$ away from r_o along a straight line tangential to the RC, along the flat diffraction grating in Fig. 1, and projected on to the Rowland mount. From this and the central path length, a half-integer number of wavelength differences at the derived order can be determined

$$\frac{2(l_l - l_c)}{m\lambda_{\text{FPR}}} = N.$$

3) Rounding N up to the nearest integer gives the first path length to be searched for along the grating line, which may be a facet center or a terminator, using

$$l_l = \frac{Nm\lambda_{\text{FPR}}}{2}.$$

4) The following search is then repeated until all the required facet centers and terminators are defined between $-L/2$ and $+L/2$.
   i) The Brent method [12] is used to find a minimum in the difference between the path l_j (or $l_{j+0.5}$) and the ideal path length $Nm\lambda_{\text{FPR}}/2$ as a function of a point positioned on the grating line at r_j (or $r_{j+0.5}$) in a range that starts at the left end of the grating or the previous facet or terminator position and extends to the opposite end of the grating.
   ii) When the error is below tolerance (1E-4 μm), we continue to the next facet center or terminator with a value of N incremented by 1.
   iii) If the path length is found to be unachievable in this range, an incrementally increasing alternating larger and smaller value of N is tested until a point is found, which satisfies l_j or $l_{j+0.5} = Nm\lambda_{\text{FPR}}/2$.This method guarantees that facets are defined along the entire length of the grating for any non-order zero grating with the center of a facet lying in the center of the grating. A diagram of the position of the central facets cardinal points is given in Fig. 2.

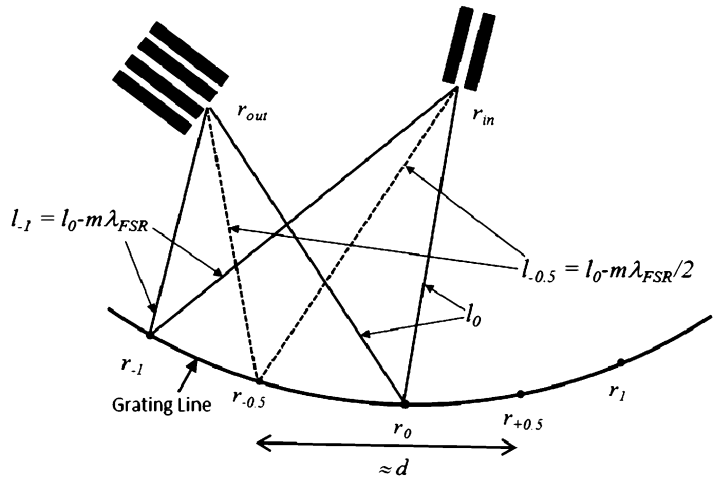

Fig. 2. Schematic showing some of the paths and the positions of the points that define the central facet.

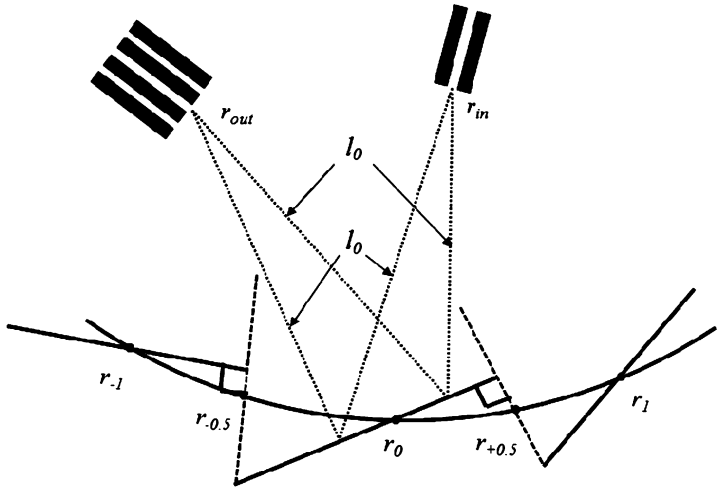

Fig. 3. Schematic of a grating showing the two paths used to determine the direction of the central facet. Also, shown is the termination line of a facet, which is done perpendicular to the facet at the right edge passing through the $r_{j+0.5}$ points.

2.2. Blazing the Facets

Choosing the direction of the facets alters the diffraction order into which the maximum intensity is focused and the quality of the beam focus. All light reflected from a given facet should ideally arrive at one point on the OutWG in phase. To achieve this, one can take two points on a line defining the front face of the facet equidistant from the center and rotate the facet until the path difference between the two points becomes zero, as shown in Fig. 3.

As well as determining the direction of a facet face, the blaze also determines the position at which a facet is terminated. The two ends of the jth facet are determined from where the facet crosses two lines normal to the $j-1$th and jth facets passing through the $r_{j-0.5}$ and $r_{j+0.5}$ points, respectively.

2.3. Curvature of a Facet

Shown in Fig. 4 is the method used for calculating the curvature on each individual facet. It was chosen to use a circular section to curve the facets with the center of curvature lying on a line

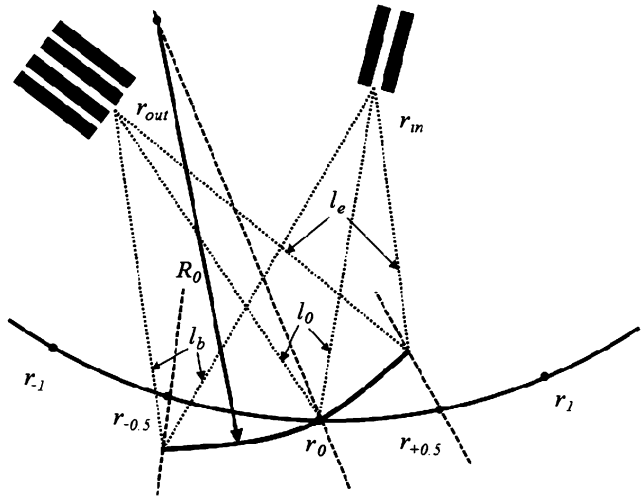

Fig. 4. Schematic showing the three path lengths l_b, l_e, and l_0 compared when defining the curvature, the radius of curvature R_j, and the two dashed lines perpendicular to the blaze of the facet.

defined normal to the facet, as blazed in the previous step, crossing the facet center and at some radius R_j. The two ends of the facet are determined by calculating the point at which this circular section crosses the terminating lines defined during blazing. The length of R_j is varied until the difference in path lengths between the beginning l_b and the end l_e of the facet with the facet center is minimized, i.e., $\Delta l = |l_0 - l_b| + |l_0 - l_e|$ is at a minimum.

3. Performance Comparison With Alternative Gratings

All the designs that follow have been compared for operation with a single slab mode of TE polarization. It is expected that any birefringence would affect all gratings designs equally and there is no benefit of one design over another. A discussion of polarization effects in the slab and at the grating facet is provided in Sections 4.1 and 4.9.

3.1. Comparison With a Standard Rowland Grating

The algorithms outlined above have been implemented in a simulator EpipProp [13]. This software uses standard diffraction theory to propagate each TE and TM slab mode of the FPR from the InWG to the grating, and the wavefront reflected back from the grating to the OutWGs. The grating is broken down into small elements, and reflection from each element is computed using Fresnel coefficients, i.e., assuming a plane-wave-like local behavior. Coupling from the modes of the InWG mode to the slab modes and from slab modes to OutWG modes is computed using vector field overlap integrals (ExH).

A series of four simulations has been run on EpipProp to simulate the effect of each step in the above grating definition and a comparison with a standard Rowland grating, with the facets projected onto the grating line from a flat grating. The four gratings are directly comparable, except for the changes to the grating through the above three steps. The four designs use a deep-etched grating interface, which has a metallized coating of aluminium to improve reflectivity. The grating is 300 μm in length with the period at the center of 7.03 μm, chosen so that the standard Rowland grating operates at the same order as the PCG at $m = 18$. The RC radius is 175 μm. The waveguides are 1.75-μm wide and deep etched. The input and output array are placed at angles $\theta_i = 48.75^\circ$ and $\theta_o = 40.5^\circ$ (see Fig. 1). There are eight OutWGs, which are spaced according to wavelength using (1) with a spacing of 5 nm around a 1550-nm central wavelength, which leads to an array with an average but non-constant physical spacing of 2.73 μm. In all simulations, power is injected into the device from the zeroth TE mode of the InWG.

TABLE 1

Epitaxy used in calculations

Material	Thickness (μm)	n_{eff} (λ=1.55μm)
Air	0.8	1
Si	0.22	3.48
SiO_2	0.8	1.445

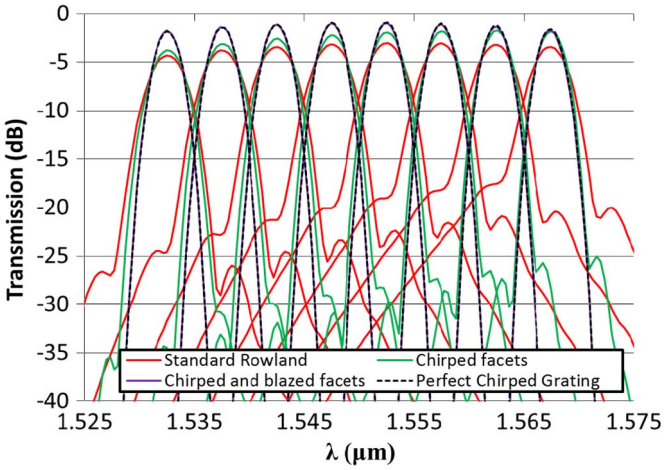

Fig. 5. Shows the three stages of optimization: chirping the facet period; chirping and blazing each facet individually; and chirping, blazing, and curving each facets. Shown also is the result from a standard Rowland mount with fixed blaze and period. Note that the chirped and blazed and the PCG differ very slightly, and hence, the latter is shown dashed on the chart.

The slab structure into which the EG is defined is typical for a SOI platform and is composed of three layers of composition and thickness, as shown in Table 1. The table shows a specific refractive index at the central frequency of operation, but the actual simulations take material dispersion into account. This slab structure supports a single TE and TM mode, and both are included in the simulation.

The four simulations separate the three stages described in the sections above and show the corresponding improvement in performance as each part of the process is introduced. From Fig. 5, it is immediately apparent that there is an improvement in the performance of the device from the chirping and blazing of the facets. The further improvement from facet curvature is quite a small effect due to the relatively short facets of this device, leading to relatively small curvature. In cases where there is a large facet size relative to Rowland radius, it has been shown that the performance can be further improved with elliptical facets [14]. In Table 2, shown is a summary of the device performance in each of the four cases.

In each of the four stages, there is an improvement in the peak transmission. However, the standard deviation in transmission of a chirped grating is worse than a standard Rowland mount until the addition of facet-by-facet blaze tuning. In summary, for this design, the PCG design gives us over 2 dB of additional transmission, and reduces the crosstalk substantially from −18 to −52 dB.

3.2. Comparison With a TSPG

In the comparison shown above of the PCG against a standard Rowland grating, the position of the waveguides and grating line is the same, and the difference lies in the definition of the grating teeth. A similar comparison is more difficult with the two stigmatic point grating (TSPG) [9], [10] as the waveguides are now defined along a straight line instead of the RC and the facets are not defined along the Rowland mount but instead via a series of overlapping ellipses [9], [15]. The

TABLE 2

Performance comparison at each optimization stage

Grating Type	Peak Transmission (dB)	Peak Halfwidth (nm)	Crosstalk (dB)
Standard Rowland	-3.39(0.44)	3.69(0.02)	-18.82(2.86)
Chirped	-2.33(0.75)	3.02(0.21)	-28.48(1.18)
Chirped and Blazed	-1.17(0.28)	2.49(0.03)	-51.1(3.12)
Full PCG Design (chirp, blaze, curve)	-1.12(0.26)	2.48(0.02)	-52.16(3.28)

comparison is therefore carried out using a fixed spacing in frequency and physical spacing of the OutWGs, fixing the crosstalk between waveguides, and the physical size of both devices. In each case, the gratings are optimized using the rules outlined in Section 4.

3.2.1. PCG and TSPG Definition

A TSPG is compared with the PCG for the following device specification. The epitaxy is as shown in Table 1. The OutWGs are deep etched, of 2.5-μm width, and their center lines are spaced, on average, 3.5 μm apart. The InWG is similarly deep etched, 2.5-μm wide, and placed adjacent to the OutWG array. Thirteen channels are spaced in wavelength by 0.003 μm around 1.5475-μm wavelength, thus covering the majority of the C-band. Both single- and multimode OutWG operation were considered. The grating was simulated with aluminium-coated facets, and each facet has been curved and blazed using the methods in Sections 2.2 and 2.3 for both gratings. The frequency and physical spacing of the output channels was used to define the position and shape of the two grating as follows.

The centers of the facets in the TSPG design were defined using the method in [9] and [15], which defines a grating based upon overlapping ellipses. The InWG is placed at the common focus of both series of ellipses at the origin, and the other two focal points were displaced along the *y*-axis by 21 and 51 μm. These positions are matched with the position of the fourth and tenth waveguides in the output array. The centers of the tilted waveguides are therefore, on average, spaced by 5 μm along the path upon which the waveguides terminate. With an incidence angle of $\approx 45^\circ$, this means that the spacing between adjacent waveguides is ≈ 3.5 μm as required. The facets were placed to produce two stigmatic points at the wavelengths of 1.5565 and 1.5385 μm at the two focal points. A grating 101 facets long was selected as this produced a grating long enough such that the length is approximately 1-w_{min} long (see Section 4.5), and the grating was chosen using the sixtieth to one hundred and sixtieth ellipse crossings that had reasonably uniform facet sizes.

The facet centers in the PCG were laid out as defined in Section 2.1. The Rowland radius was calculated to be 466 μm using (4) (see Section 4.2) with the OutWG physical and wavelength spacing for a grating with InWG and OutWG positioned at 45.5° and 48°, respectively. The angles were chosen such that the whole output array, which is terminated on the RC, could see the whole grating. The grating length was chosen to be 622 μm, approximately 1-w_{min} long (see Section 4.5).

The OutWGs in the case of the TSPG were spaced according to simulations run at each OutWG central wavelength. The position of the peak at the two tuned wavelengths is fixed by construction, but the position of the other waveguide channels changes depending on the chosen ellipse crossings taken to define the grating facet positions. As such, a simulation at the desired wavelength for each OutWG was undertaken and the waveguide position adjusted to match the resultant peak position. This leads to uneven waveguide positioning with OutWGs centered at shorter wavelengths, being closer together than those at longer wavelengths. It is worth noting that without this simulation and tuning step, the resulting spectra for a device will have the peaks at the higher wavelength end closer together, as can be seen in the results from [9] and [15].

The positions of the OutWGs in the case of the PCG were defined using (1) and the desired wavelength for each guide. This leads to an average spacing of 5 μm along the RC. The incidence

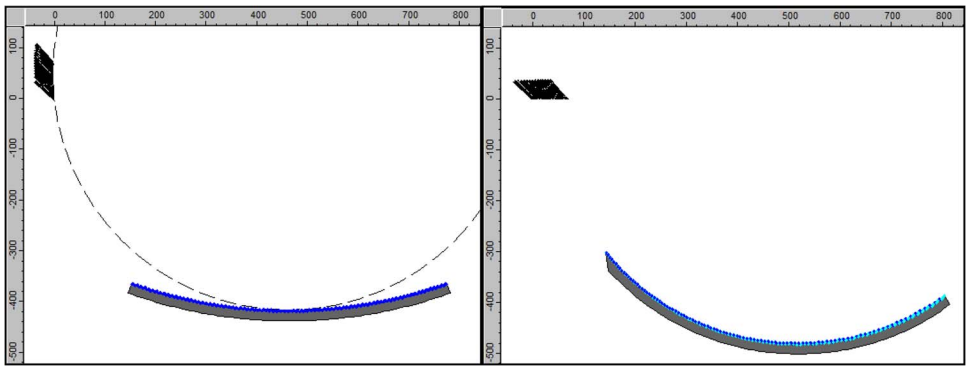

Fig. 6. Shown are the gratings as used in the simulation, (left) PCG and (right) TSPG. Both gratings are displayed on the same size scale in micrometers with the origin placed on the center of the InWG with the last 50-μm length shown for all waveguides before entering the FPR.

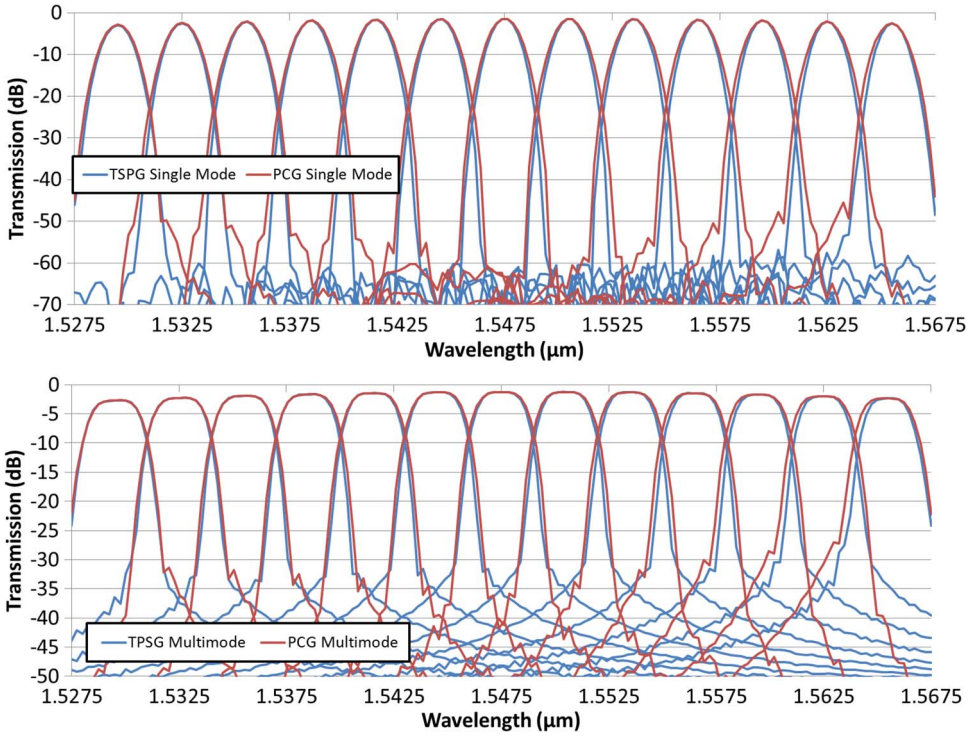

Fig. 7. Showing the comparison between the TSPG and the PCG for the two optimized devices with single-mode InWG: (top) single-mode OutWGs and (bottom) multimode OutWGs.

angle of the center of the OutWGs being 45.5° leads to the spacing between adjacent waveguides of $\approx$3.5 μm as required.

The resulting grating designs are shown in Fig. 6. Both designs are almost comparable in size if one takes the waveguides and grating into account with the footprint being approximately 500 μm $\times$ 800 μm. The simulations were carried out in EpipProp[13] with the same resolution with multiple grating to grating reflections included.

3.2.2. Results

Shown in Fig. 7 are the resulting spectra from the two simulations and in Table 3 are the summarized results. As expected, the performance in multimode operation in both cases leads to

TABLE 3
Shows the comparison between results of the PCG and the TSPG

Grating Type	Peak Transmission (dB)	Peak Half-width (nm)	Crosstalk (dB)	Worst Case Crosstalk (dB)
TSPG Single Mode	-1.93(0.46)	1.14(0.03)	63(3)	55
PCG Single Mode	-1.89(0.44)	1.251(0.005)	61(4)	52
TSPG Multimode	-1.72(0.46)	2.25(0.1)	33(1)	30
PCG Multimode	-1.72(0.46)	2.405(0.003)	36(3)	29

a slightly enhanced transmission while almost doubling the half-width of the device (see Section 4.6). The crosstalk between neighboring waveguides is, on average, better for the PCG in multimode operation and the TSPG in single-mode operation. However, the standard deviation in crosstalk is slightly worse in the case of the PCG in the multimode case, which reflects that the PCG either outperforms or is equivalent to the TPSG in 9 out of the 13 channels but underperforms at longer wavelength. The half-width is broader in both the single- and multimode operation of the PCG but with much less variability while maintaining the same peak transmission as with the TSPG. The TSPG starts with widths comparable to the PCG at low wavelengths with the peak width reducing as the wavelength increases, showing a gradient in the focusing of the device along the OutWG.

In general, both devices have been successfully optimized using the rules laid out in Section 4 and perform very comparably for equally spaced waveguides, physical and wavelength, and device size. The PCG device shows an improved behavior over the TSPG device in the more uniform channel width in both the single- and multimode operation. However, the maximum crosstalk in the waveguides at the edges of the OutWG array is typically a few decibels better in the TSPG than in the PCG.

4. Optimizing an EG

Optimizing any WDM device is always a matter of compromises depending on the materials and the tools available. What follows is a description of different parameters associated with a grating and what must be considered in each case. This list has been created using a particular PCG design but can be applied to all EG designs.

4.1. Diffraction Order

An EG will couple multiple wavelengths to the same OutWG. The spacing between these wavelengths is termed the free spectral range (FSR) and decreases with increasing grating order m. Clearly, for usual WDM uses, the FSR must be larger than the range of wavelength channels. This sets a maximum allowed grating order for the required spectral range $\lambda_+ - \lambda_- = \Delta\lambda$, where λ_+ and λ_- are the wavelengths associated with the outermost waveguides, which is

$$m_{\max} < \frac{\lambda_- n_+}{\lambda_+ n_- - \lambda_- n_+} \tag{2}$$

where $n_\pm = n_{\text{eff}}(\lambda_\pm)$ is the effective index of the FPR slab mode at these wavelengths.

From this, one can see that the actual maximum value of $m_{\max}$ not only relies on the wavelength range but also on the effective index and its dispersion $dn_{\text{eff}}/d\lambda$. This differs from the usual definition [16] of $m_{\max}$, which ignores any effective index dispersion and gives $m_{\max} = 31$ in the case of a 50-nm range at 1.55 μm in the epitaxy in Table 1, as opposed to using (2), which gives $m_{\max} = 23$.

Rule 1: Choose an order of grating such that the FSR is greater than the spectral range of your device.

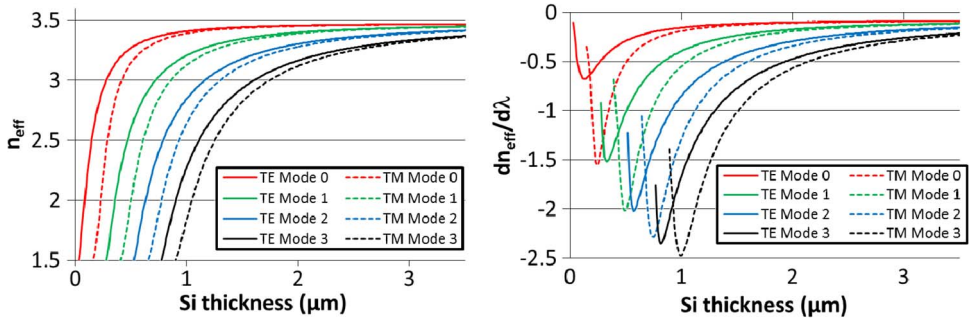

Fig. 8. Shown are the calculated values of $dn_{\text{eff}}/d\lambda$ and $n_{\text{eff}}(\lambda)$ for the first four slab modes at 1550 nm in a slab with a base of 0.8-μm-SiO_2, the shown thickness of Si, and a top layer of 0.8-μm air. Note that the order increases from left to right, and data are not included where the slab modes are not guided.

4.2. Position of Waveguide Arrays

One can derive the linear dispersion along the RC from (1) giving

$$\frac{ds}{d\lambda} = \frac{R\left(1 - \frac{dn_{\text{eff}}}{d\lambda}\frac{\lambda}{n_{\text{eff}}(\lambda)}\right)}{n_{\text{eff}}(\lambda)\left(\left(\frac{d}{m}\right)^2\cos^2(\theta_i) + \frac{d}{m}\frac{\lambda}{n_{\text{eff}}(\lambda)}\sin(\theta_i) - \left(\frac{\lambda}{n_{\text{eff}}(\lambda)}\right)^2\right)^{\frac{1}{2}}}$$

where R is the radius of the RC. The ratio d/m is fixed for a specific grating by the choice of the InWG and OutWG array positions and wavelength of operation through

$$\frac{d}{m} = \left(\frac{n_{\text{eff}}(\lambda_c)}{\lambda_c}(\sin(\theta_i) + \sin(\theta_o))\right)^{-1}. \tag{3}$$

In asymmetric slab structures, such as SOI, the $dn_{\text{eff}}/d\lambda$ of a mode within a slab waveguide is negative and will peak at a core thickness close to cutoff, as shown in Fig. 8 for the first four supported SOI slab modes. This peak will combine with the lower effective index to further enhance the spatial dispersion and allow a smaller device.

Rule 2: Optimize slab design to maximize $dn_{\text{eff}}/d\lambda$ and minimize n_{eff}.

To take advantage of the focusing from a Rowland mounting, one must place all the InWG and OutWG on the RC. This means that the relative spacing between waveguides when projected onto the RC will be larger than the inter-waveguide spacing s_{RC} and vary as a function of the angle (see Fig. 9). The OutWG spacing along the RC is thus

$$s_{\text{RC}} = \frac{s_{wg}}{\cos(\theta_o)}$$

s_{RC} can be directly related to the dispersive behavior of the grating, and this allows the required s_{wg} to be calculated for a specific epitaxy, θ_i, θ_o, λ, R, and channel spacing $\Delta\lambda_{\text{chan}}$ through

$$s_{wg} = s_{\text{RC}}\cos(\theta_o) = \frac{ds}{d\lambda}\Delta\lambda_{\text{chan}}\cos(\theta_o). \tag{4}$$

Shown in Fig. 10 is a plot of $s_{wg}/R\Delta\lambda_{\text{chan}}$ versus θ_o and θ_i, which shows the required spacing of the OutWGs normalized to the channel wavelength spacing and the Rowland radius. A larger value of $s_{wg}/R\Delta\lambda_{\text{chan}}$ implies that a smaller RC can be used to get the same dispersive behavior for specified channel spacing. It is clear that placing both the InWG and OutWG at the same angle, i.e.,

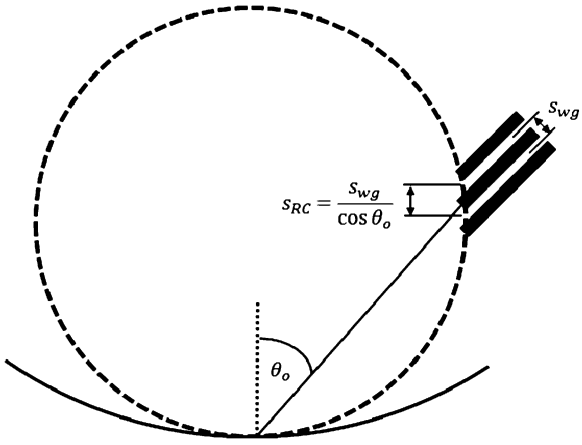

Fig. 9. Schematic of an RC showing the position of an OutWG array with interguide spacing of s_{wg} and spacing projected onto RC of s_{RC}.

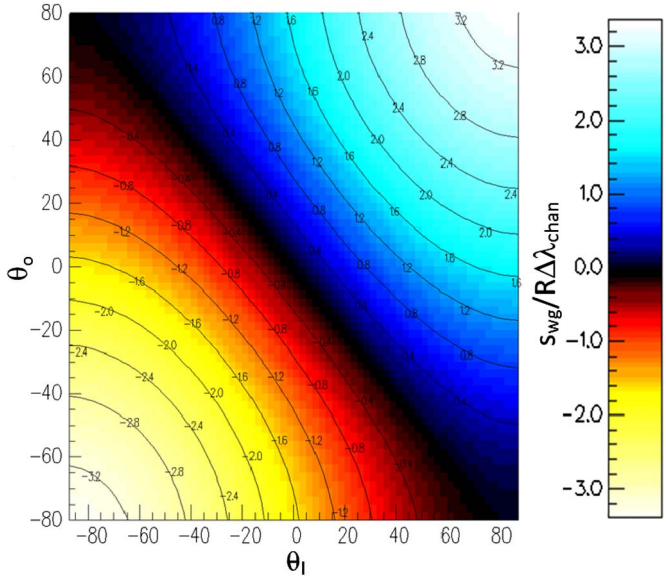

Fig. 10. Shows $s_{wg}/R\Delta\lambda_{chan}$ at 1550 nm in a slab waveguide described in Table 1 as a function of θ_o and θ_i relative to the grating normal. Note that the plot is in units of micrometers.

$\theta_o = \theta_i$ and overlapping, gives the best dispersive behavior and that placing them at a greater angle on the same side of the normal to the grating also improves performance. For practical reasons, the InWG and OutWGs do not overlap, and the OutWG array will have a finite width, meaning the spacing between each individual waveguide should be tuned to the intended wavelength as dispersion varies around the RC. To get the best dispersive response in a fixed epitaxy, and hence the smallest device, we therefore have the following rule:

Rule 3: Place the InWG as close to the OutWGs and at the largest practical angle.

4.3. Polarization Effects

It is worth mentioning that in a DWDM receiver, the incoming light is generally unpolarized. The different effective indices of the TE and TM modes of the EG slab region result in an unwanted shift in the transmission spectra and insertion loss between the two polarization states.

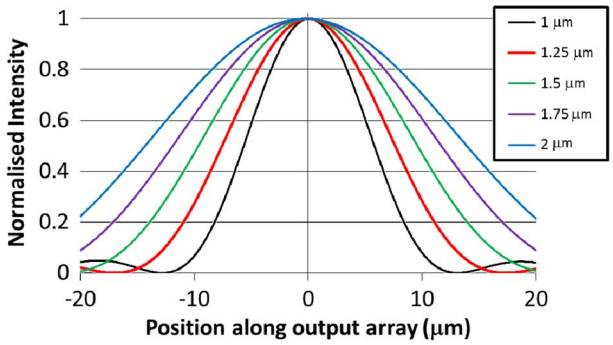

Fig. 11. Shown is the normalized intensity from a single facet associated with $W = 8.34$ nm, for wavelengths from 1 to 2 μm.

As can be seen in Fig. 8, one partial solution to this is to use thicker core layers in the epitaxy, for instance, using Si layers thicker than 3 μm, where the effective index and $dn_{\text{eff}}/d\lambda$ of the TE and TM modes of each order converge. In such structures, the disparity in the effective index between modes of the same order but different polarities will lead to small variations in the position of their respective diffraction orders. The disadvantage to such an approach is that the slab waveguide now supports many multiple modes of the same polarization, each with a slightly different effective index. To avoid coupling between these modes, the verticality of the grating facets, waveguide etchs, and/or multimode behavior in the waveguides has to be more strictly controlled. These fabrication errors can be compensated through waveguide positions, as in [4], but such methods require small θ_I and θ_o and therefore larger devices.

A more complete approach to dealing with plurality in polarization in the slab region can be done using a wedge-shaped change in the epitaxial structure in the FPR between the InWG/OutWG and the grating (see, for instance, [17]–[19]). With this method, any grating design can be combined with two appropriate FPR regions to compensate for birefringence in the FPR.

4.4. Period of a Grating/Facet Size

The facet size has a strong effect on the efficiency of an EG with wavelength. The light diffracted from an individual facet will give a distribution of intensity at the output of the form expected from diffraction from a single slit

$$I_{\text{facet}}(\theta) \propto \text{sinc}\left(\frac{W}{2}k_b(\theta)\right)^2 \tag{5}$$

where $k_b(\theta) = 2\pi(n_{\text{eff}}/\lambda)\sin(\theta - \theta_o)$, θ is the angle from the normal of the grating, and W is the facet width; this facet is assumed to be blazed such that reflected light arrives at the center of the OutWGs θ_o. One can also write down the intensity scattered from a simple grating as

$$I_{\text{grating}}(\theta) \propto I_{\text{facet}}(\theta)\left(\frac{\sin\left(N_F k(\theta)\frac{W+d}{2}\right)}{\sin\left(k(\theta)\frac{W+d}{2}\right)}\right)^2$$

where N_F is the number of facets, and $k(\theta) = 2\pi(n_{\text{eff}}/\lambda)\sin(\theta)$. This simplistic representation ignores the focusing effect and any aberrations of a curved grating but is still informative. From these two, one can immediately see that the intensity of diffraction at a specific angle will be contained within the envelope of that from a single blazed facet. Shown in Fig. 11 is the intensity across a path defined along the RC from a simulation run in EpipProp of a single facet of fixed size but with varying wavelength.

As can be seen from (5), the size and shape of the envelope is a function of the wavelength and width of the facet. In most applications, $\Delta\lambda$ is small compared to λ_c, and the envelope is determined

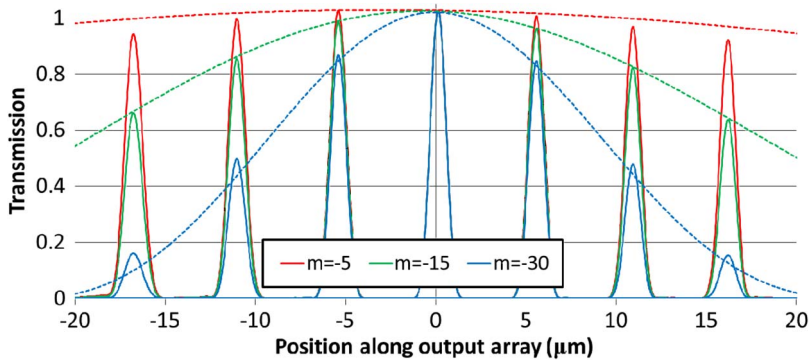

Fig. 12. Shows the intensity peaks at seven wavelengths along the OutWG array of an EG of fixed length and the wide envelope associated with the intensity from a single facet at 1.55 μm, normalized to the intensity of the central peak.

more by the size of the facet. Shown in Fig. 12 is the intensity at the OutWG array from seven wavelengths spaced apart by 10 nm around a central wavelength of 1550 nm with fixed waveguide positions and varying the order m by changing the period d. The change in d affects the width of the facet, i.e., W with the width of the central facet of a grating given by

$$W = d\cos\left(\frac{\theta_i + \theta_0}{2}\right).$$

From this, it is seen that the peak intensity in the center of diffraction is theoretically not dependent on the facet size or the order, but the variation of intensity with wavelength is highly dependent on the facet size and, hence, on the position of the waveguides and the order of choice. This leads to

Rule 4: Use shorter facets to minimize the variation in transmission between WDM channels.

This also highlights the importance of blazing the facets correctly. If the facets are incorrectly blazed, not only will it affect the shape of an individual wavelength peak but it will also alter the shape of the envelope around all the peaks. If for instance the blaze angle is, on average, off-center, a slope in the peak intensity away from the center will be apparent. This is shown in Fig. 13, where the response of a non-optimally blazed grating is shown.

Rule 5: Optimize the blaze of each facet to improve uniformity in wavelength performance.

4.5. Size of Waveguide Mode Profiles and Spacing of Waveguides

This shape of a mode in a 2-D confined waveguide is determined by the waveguide dimensions, the refractive index step at the edges, and the wavelength of light. One can modify the shape of a mode profile at a fixed wavelength by adjusting the width and height, through choice of epitaxy, and the etch depth or doping at the edge. With an accurate model of the system, one can partially tune a mode profile to get a desired shape.

As the magnification of a Rowland-based mounting is theoretically one to one, the overlap of the image of the input and output modes can be given as adapted from [8]

$$O(\Delta\lambda) = \int A_{\text{Output}}(x, y) A_{\text{input}}\left(x + \frac{ds}{d\lambda}\Delta\lambda, y\right) dx\, dy \tag{6}$$

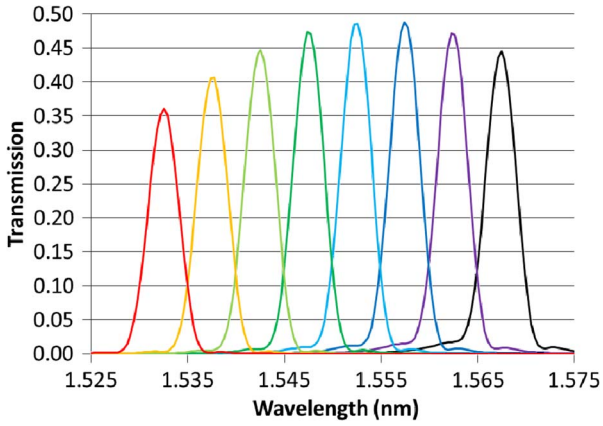

Fig. 13. Shown is the spectral response from the standard Rowland grating as described in Section 3.1 without any optimization. The peak shape is poor due to poor positioning and blazing of the facets. The poor blazing has also lead to an envelope whose peak is shifted toward higher wavelengths.

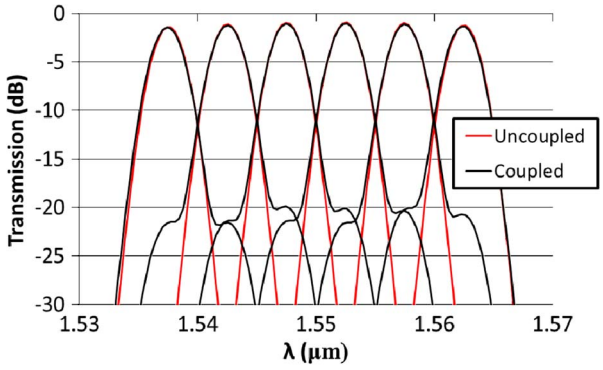

Fig. 14. Shows the spectrum of a device with and without including the coupling between nearest neighbors (introduced by using a link between EpipProp [13] and FIMMPROP [20]).

where $O(\Delta\lambda)$ is the overlap of the modes with respect to changing wavelength of a perfectly tuned grating (with a value of 1 if $\Delta\lambda = 0$ and the mode profiles at the InWG and OutWG are the same) and A_{Output} and A_{Input} are the amplitude of the mode profile at the InWG and OutWG, respectively, projected onto the interface between the FPR and OutWGs. The integral is performed at the interface between the FPR and the OutWG and ignores any aberrations in the grating focusing.

Looking at (6) gives an insight into the geometry considerations of the mode profiles at the InWG and OutWG of the echelle device and highlights how they will affect crosstalk through the following:

1) The broader the mode profile of the OutWG, the further apart one has to place the OutWGs and the higher the dispersion will be required for a specific $\Delta\lambda_{\text{chan}}$.
2) The broader the image of the InWG mode at the output array, again the larger the dispersion and OutWG spacing required.
3) For maximum transmission, the image of the InWG mode should match the OutWG mode profile.

The shape of the modes will be determined by the properties of the waveguide. A large index contrast at the walls of a waveguide will confine the mode more strongly and thus allow waveguides to be placed closer together and require less dispersion and thus a smaller device in the same epitaxy.

A second important addition to crosstalk, which is often neglected, can come from the effect of coupling between waveguides in the OutWG array. Shown in Fig. 14 is the spectrum for the PCG

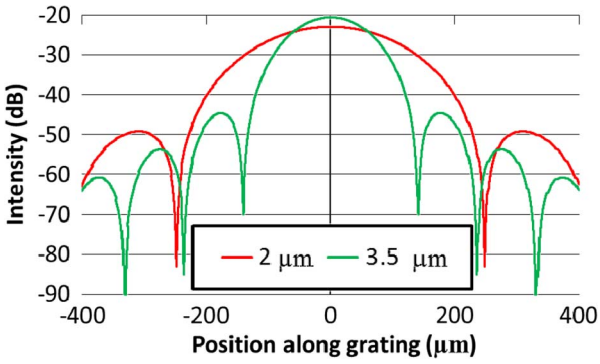

Fig. 15. Shows the intensity along a grating 800-μm long caused by a deep-etched single-mode InWG of 2- and 3.5-μm wide incident normal to the grating across an RC 300 μm in radius.

device outlined in Section 3.1 with six shallow-etched OutWGs, of 30-nm etch depth, with and without nearest-neighboring coupling. The best way to check for such a situation is to model the waveguides after the coupling from the FPR and see if there is any coupling between them as they taper away from one another and/or taper in width. This sort of effect has been seen in [3] and the results in [9], but we believe that this is the first EG model with inter-waveguide coupling included.

In general, one must always choose a tradeoff in the spacing of the OutWGs, to reduce cross channel coupling, and the size of the device required to achieve the required dispersion.

Rule 6: To minimize crosstalk, ensure that the OutWGs are spaced sufficiently such that the image of the input mode profile does not overlap with adjacent output channels.

Rule 7: Ensure that the OutWGs are sufficiently decoupled such that inter-waveguide coupling does not lead to crosstalk.

4.6. Length of Grating

The resolving power of a diffraction grating is given by [16]

$$R_p = \frac{\lambda}{\Delta\lambda} = mN_F = \frac{Ln_{\text{eff}}(\sin(\theta_i) + \sin(\theta_o))}{\lambda}$$

where L is the length of the grating. This result shows that the resolving power of an EG for a specific wavelength range is related to the length of the grating and the position of the InWG and OutWG. This also assumes uniform illumination and does not take into account any de/focusing of the light from the shape of the waveguides and grating. In practice, it is the width of the waveguides that often limits the resolution.

The divergence of a beam when entering the FPR will be $\propto \lambda_{\text{FPR}}/w_{\text{input}}$, where w_{input} is the width of the InWG mode, and the quantity of light interacting with the grating will be defined by the solid angle subtended by the grating, which is $\propto w_{\text{grating}}/R$, where w_{grating} is the width of the grating. The actual form will be very dependent on the shape of the mode profile and the chosen angle of incidence.

Using EpipProp [13], one can examine the shape of the beam at the grating. Shown in Fig. 15 is the intensity received at a grating from two different waveguide widths. Note the minima in these profiles, which is typical of a strongly confined waveguide. One can define a width w_{min} for the length of a grating associated with capturing the entirety of the first diffraction peak from the input. As can be seen in Fig. 15, in this geometry, w_{min} is 496 and 282 μm for a waveguide width of 2.0 and 3.5 μm, respectively, for a $\lambda = 1.55$ μm.

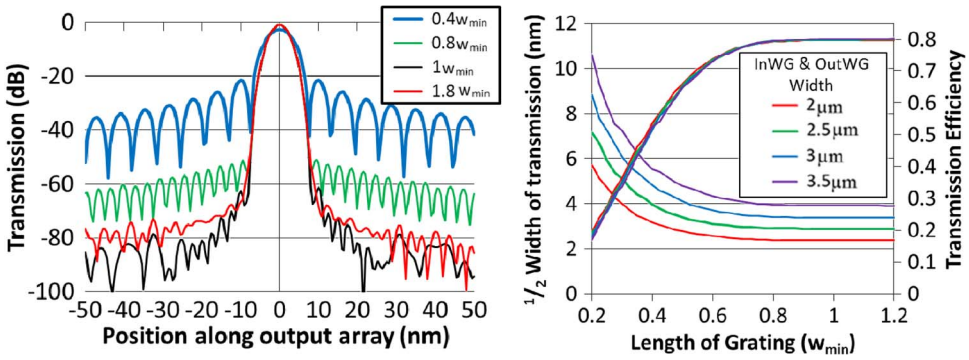

Fig. 16. Shown above (left) is the response of an OutWG of 2.0-μm width shifted along the output array to a 2.0-μm wide InWG, both with varying grating length normalized to w_{min} and (right) the transmission efficiency and half-width to an OutWG from an EG. The half-widths were determined from scans similar to those shown left, for four different InWG widths.

Shown in Fig. 16 is (left) a plot of the transmission efficiency between an InWG and an OutWG of the same dimensions and (right) the 1/2 width of the response from a grating of various lengths normalized to w_{min}. Under this normalized length, the transmission efficiencies of all waveguide widths overlap. The transmission efficiency and the half-width vary strongly with length until 0.8 w_{min}. There is also an improvement in the noise floor, as shown in the left in Fig. 16, if one uses a grating of 1.0 w_{min}. Beyond this length, very little improvement in the device is seen, and the performance can actually degrade as any aberrations associated with the shape of the grating will be more prevalent in a larger device (see, for instance, 1.8 w_{min} in Fig. 16 left). As expected, the 1/2 width of the transmission curve is directly proportional to the size of the InWG once the grating extends beyond 1.0 w_{min}.

From these results, another rule can be given.

Rule 8: Grating length should be at least 0.8 w_{min} **in order to achieve low crosstalk and maximize transmission.**

4.7. Flat-Top Response

The coupling from the image of a single-mode InWG combined with a single-mode OutWG profile will always lead to a peaked response [see (6)]. A change must be made to either the waveguides or the focusing of the grating itself to achieve a flattening of this response. Three are highlighted here.

1) MMI [14], [17] on the input. A single input mode is introduced centrally into an MMI section exciting multiple odd modes that propagate along the length of the guide. At an MMI length given approximately by [21]

$$L_{MMI} = \frac{3\pi}{8(\beta_0 - \beta_1)}$$

where β_0 and β_1 are the propagation constants of the first two modes in the MMI, the phases of the multiple odd modes match up to produce two images of the input mode equally spaced either side of the center of the MMI. Tuning the width of the MMI controls the spacing between these two images. For small MMI widths, the images overlap, leading to a broadened peak with reduced peak intensity [22]. As the width of the MMI is increased, the two images will overlap less until two independent images are produced, each an image of the input mode with half the integrated intensity. As can be seen from (6), broadening the shape of A_{input} will lead to coupling over a broader range of wavelengths, but the mismatch in shape between A_{input} and A_{output} will cause an increase in the insertion loss. A series of calculations was

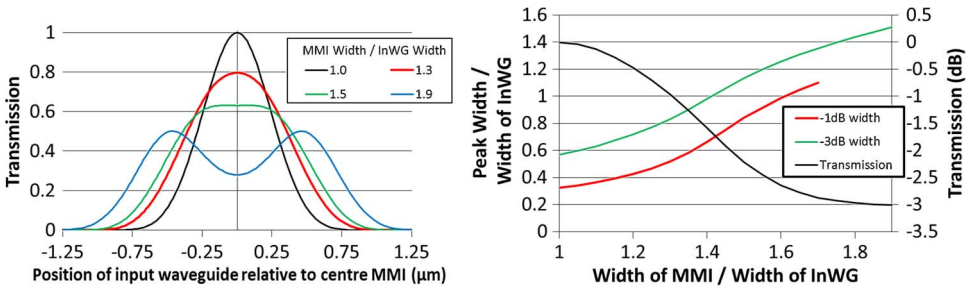

Fig. 17. Shown left is the shape of the coupling for an MMI with different peak transmission losses, and shown right is the change in peak transmission (right scale) and the −1- and −3-db widths relative to the width of the waveguide (left scale). The simulations were run using FIMMPROP [20].

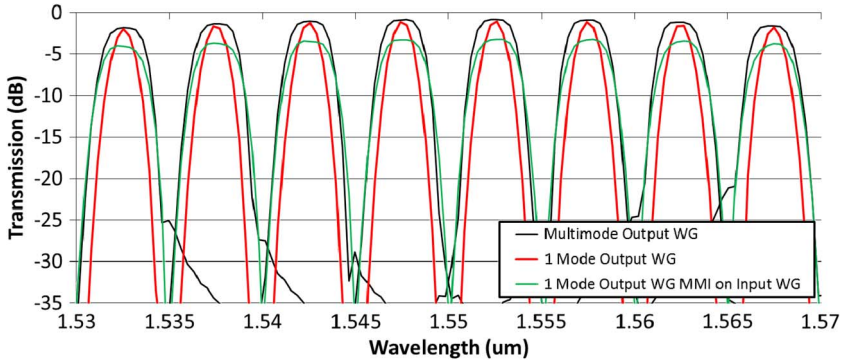

Fig. 18. Shows a comparison between 1) single-mode InWG and the sum of all modes in multimode OutWGs, 2) single-mode InWG and a single-mode OutWG, and 3) a single-mode InWG fed through an MMI tuned to the two peak point with a width 1.5× the InWG width coupled to a single-mode OutWG.

undertaken in FIMMPROP [20] with an InWG coupled centrally to an MMI that is then coupled to an identical OutWG. The two waveguides and MMI are deep etched and the MMI length tuned to the two image point. The coupling between the zeroth mode in the InWG and OutWG was calculated as the OutWG is scanned across the MMI, effectively modeling the dispersive effect of a diffraction grating with wavelength, for a series of different MMI widths. Shown on the left in Fig. 17 is the transmission from four different MMI widths, which is labeled according to the ratio of the InWG width to the MMI width, and on the right is the variation of the peak transmission and the −1- and −3-dB widths in terms of the width of the InWG. As can be seen in the left plot, the transmission peak top remains relatively flat until the MMI has a width of ≈1.5 InWG width and the peak performance has dropped to 0.63 (−2 dB). Further widening of the MMI introduces a saddle in the transmission, which becomes more pronounced such that, at around ≈1.7 InWG width, the −1-dB width is no longer meaningful as the peak in transmission has split into two peaks with the saddle below −1 dB. The same is true for the −3-dB width at ≈1.9 InWG width. The peak transmission drops to −3 dB, as would be expected for two separate images of the InWG, each with half the integrated intensity of the input.

2) Using multimode OutWGs, as in [4], [23], and [24], but this only works in a receiver.
3) The shape of the spot at the output can also be modified by changing the reflectivity and position of the grating teeth modulating the phase and intensity at the grating to be the Fourier transform of the desired output profile shape [25], [26]. Such a manipulation will lead to a flat passband response with sharp transitions, but the flat top once again comes at the expense of increased insertion loss.

Shown in Fig. 18 is the spectrum from an a EG, which is the same as the PCG described in Section 3.1 but with double the grating length and RC radius, which is simulated in EpipProp [13],

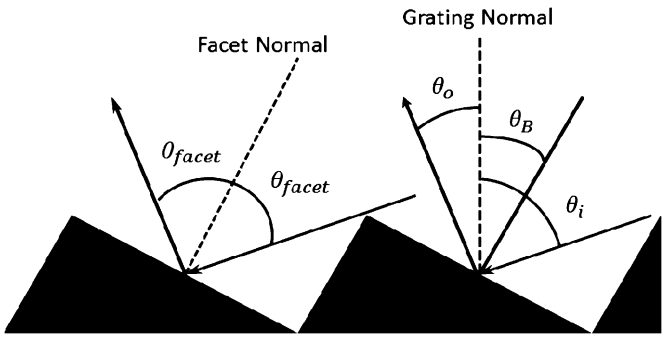

Fig. 19. Shows the definition of angles at the central facet.

showing the following: 1) the behavior with multimode OutWGs with a single-mode InWG; 2) single-mode OutWGs from a single-mode InWG; and 3) an MMI on the InWG and single-mode OutWGs. The MMI was tuned to have a -1-dB width over 80% of the OutWG with a corresponding insertion loss of -2 dB. The shape of the MMI and the multimode OutWG response is very similar on the peak, with the MMI having an additional ≈ -2-dB loss. The multimode waveguide, however, shows more noise in the tails as any signal arriving at the waveguide will couple into one of the multiple modes.

4.8. Blaze Angle of Grating, Shadowing, and Single TIR Facets

In the perfect stigmatic grating, every facet is blazed at a slightly different angle depending on the position of the center of the InWG and OutWG arrays. Even then, some parts of the facets will be shadowed from either the InWG or OutWG. In the center of the grating, one can define a blaze angle for the central facet as $\theta_B = (\theta_i + \theta_o)/2$ (see Fig. 19). One can also define θ_i and θ_o in terms of the blaze angle and an angle of incidence to this central facet, i.e., θ_{facet}, as $\theta_i = \theta_B + \theta_{\text{facet}}$ and $\theta_o = \theta_B - \theta_{\text{facet}}$.

The amount of the reflection lost to shadowing from a facet at the center of the grating can be determined from these two angles through simplistic ray tracing, ignoring edge diffraction, as

$$I_r(\theta_B, \theta_{\text{facet}}) = I_0(\theta_{\text{facet}})(1 - \tan\theta_B \tan\theta_{\text{facet}})$$

where $I_0(\theta_{\text{facet}})$ is the expected reflection from a single facet without shadowing and can be directly related to the Fresnel coefficients of reflection (see, for instance, [11]). The behavior of $I_0(\theta_{\text{facet}})$ will follow that of the material at the facet interface. For a single shadowed facet, one would expect the effect of shadowing to get worse with increased θ_B and θ_{facet}. However, the performance of $I_0(\theta_{\text{facet}})$ can greatly improve if θ_{facet} is greater than the critical angle θ_c as total internal reflection (TIR) occurs.

When one takes into account all the facets, the intensity will behave differently but can be fitted with a function of a similar form

$$I_{grat}(\theta_B, \theta_{\text{facet}}) \approx \beta I_0(\theta_{\text{facet}})(1 - \alpha\tan\theta_B \tan\theta_{\text{facet}}) \tag{7}$$

where α and β are functions of the geometry of the grating to take into account the total illuminated area and the deviation of the angle of blazing and incidence at each facet position from that occurring at the central facet, i.e., at θ_B and θ_{facet}.

A series of simulations was run to investigate the effect of shadowing in a device with one InWG and one OutWG with varying θ_B and θ_{facet}, via θ_i and θ_o, on two types of grating interface, namely, Si-aluminium and Si-air, on a PCG. These were run with a grating 280-μm long, which is chosen so that $w_{\text{min}} = 1$ was kept at all blaze angles, with an RC 300 μm in radius and with InWG and OutWG 3.5-μm wide and deep etched in the epitaxy shown in Table 1.

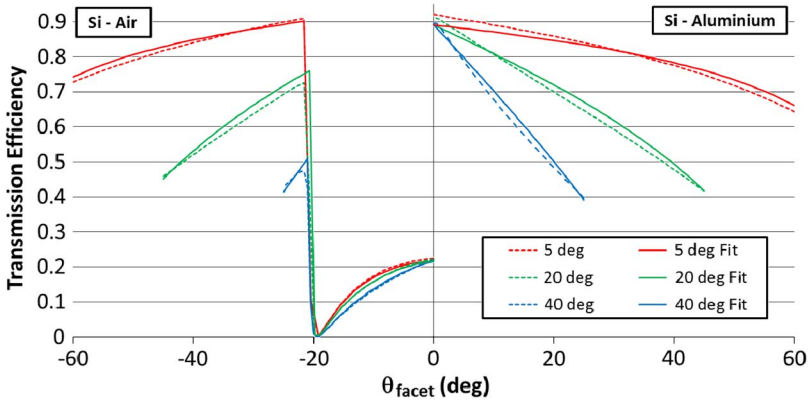

Fig. 20. Shows the behavior of a grating at three different θ_B, denoted in the legend, at a variety of θ_{facet} for a Si-air and a Si-aluminium grating interface at negative and positive angles, respectively, since the response is symmetric in θ_{facet}. With each data set is a fit to (7) with α and β constant for both materials.

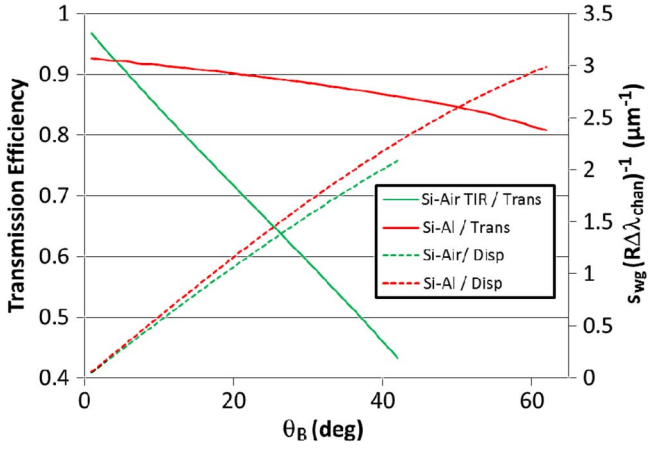

Fig. 21. Shows the transmission with blaze angle for a TIR grating with θ_{facet} fixed at 23°, sufficient such that all facets undergo TIR, and a metal grating with $\theta_{\text{facet}} = 2°$ and the related $s_{wg}/R\Delta\lambda_{\text{chan}}$ with each geometry.

The size of the facet and order was chosen to keep the period at the center of the grating close to 16 μm, through tuning using (3), while maintaining a diffraction order centered on the OutWG as θ_{facet} was varied over its range. The range in θ_{facet} was reduced as the blaze angle was increased to avoid the waveguides, terminated on the RC, occluding the grating (as can be seen in Fig. 9 if one imagines using a large θ_o). As such, the simulation was limited to $|\theta_i|$ and $|\theta_o|$ less than 65°.

The results of these simulations are shown in Fig. 20 along with a fit to (7). The fit was performed on the data collected for both the Si-air and Si-aluminium interfaces over all θ_B and θ_{facet}, giving a value of $\alpha = 0.948$ and $\beta = 1.43$ with a normalized-root-mean-square-deviation per point of 2.6%, showing a good fit to the data. This fit is shown in Fig. 20 showing that the performance can be approximated well by (7). It is worth mentioning that there is some disparity in behavior, which could be caused by the minor variation in illumination of the grating that occurs with θ_i. As can be seen in Fig. 20, the effect of shadowing with θ_{facet} becomes much more pronounced as the angle of θ_B increases.

Shown in Fig. 21 is the value of $s_{wg}/R\Delta\lambda_{\text{chan}}$ and the transmission efficiency in Si-air at $\theta_{\text{facet}} = 23°$ (for a TIR design) and Si-Al with $\theta_{\text{facet}} = 2°$ (for metallized grating) with varying θ_B. Devices using TIR will allow large reflectivity and transmission to be achieved without using any

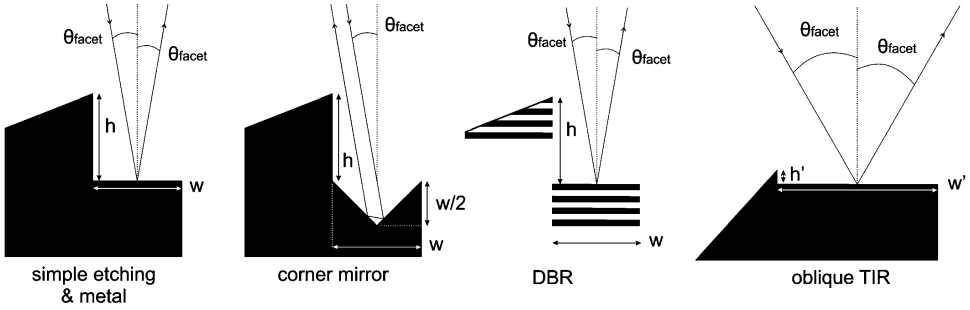

Fig. 22. Shows facet geometries used in the FDTD simulation, including the tilt on the neighboring facet introduced to send reflected intensity from this facet away from the detector. The dark areas correspond to the etched regions.

TABLE 4
Dimensions of the facets

Parameter	Value	Parameter	Value
h	4.94μm	**h'**	0.64μm
w	5.01μm	**w'**	7.23μm
θ_{facet}	-20° to +20°	θ_{facet}**(TIR)**	30°
Duty cycle (etched fraction of period)	49%	**DBR Period**	0.795μm

additional material or etching process. However, the size of the devices will have to be bigger as the benefits gained in reflectivity will be lost in the dispersive behavior. For example, a device using TIR with high transmission (-0.94 dB) with a blaze at 13° and $s_{wg}/R\Delta\lambda_{chan}$ of 0.70 μm^{-1} can be compared with an aluminium reflective interface with the same transmission with a blaze of 62° and an $s_{wg}/R\Delta\lambda_{chan}$ of 2.99 μm^{-1}. The performance in both devices would be the same, but the metal-coated device would have an RC $\approx$ 4 times smaller, and with the larger angle of approach of both the InWG and OutWG requiring only half the RC, the actual total foot print of the device would be at least 32 times smaller.

This leads to another rule.

Rule 9: To minimize the insertion loss due to shadowing, one should keep the InWG and OutWG close together, minimizing θ_{facet}, and/or keep the blaze angle θ_B small.

4.9. Choice of Facet Type: FDTD and Shadowing

Another aspect in the design of any grating is the choice of facet type. In this section, an investigation into five common facet types (plain deep etch, metallized facet using silver, distributed Bragg reflector (DBR), corner mirror, and oblique TIR) was performed using a finite-difference time-domain (FDTD) [27] tool. The reflectivity and scattering of these facet geometries were compared for a range of θ_{facet} from $\pm 20°$ at a fixed $\theta_B = 44.625°$, except in the case of the oblique-TIR facet, for which $\theta_{facet} = 30°$ and $\theta_B = 5°$. The FDTD calculations were performed in 2-D in both TE and TM polarizations, the vertical direction being approximated through the use of an effective index of 2.85 (equivalent to that of a TE slab mode in the structure described in Table 1).

In order to model the effect of neighboring facets, the reflectivity was measured for a single facet considered (a) on its own and (b) in the presence of its first neighbor. The orientation of the neighboring facet was modified so that it would not reflect light in the direction of specular reflection, allowing us to characterize the effect of scattering and shadowing. The geometries are described in Fig. 22 and Table 4.

TABLE 5

Comparison of the reflectivity for the different facet types individually and in the presence of a neighbor

Facet Type	Reflectivity TE (single facet)	Reflectivity TM (single facet)	Reflectivity TE (single facet with neighbour)	Reflectivity TM (single facet with neighbour)
Simple Etch	24.1%	23.8%	19.6%	24.8%
Metalised	99.7%	96.3%	76.5%	88.7%
DBR	98.4%	97.2%	91.3%	90.6%
Corner	78.4%	80.2%	79.5%	81.2%
Oblique-TIR	95.0%	94.4%	90.4%	89.7%

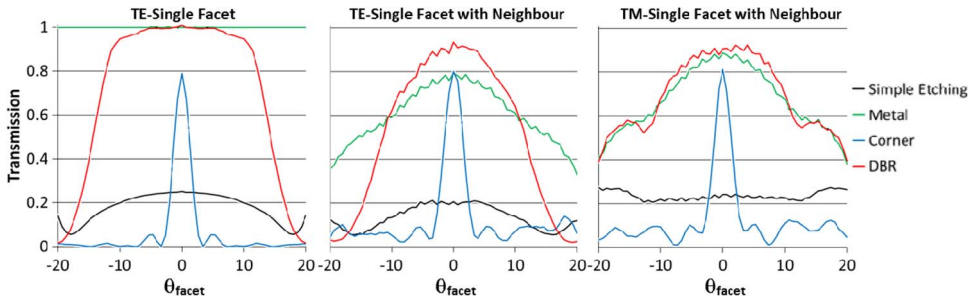

Fig. 23. Comparison of the reflectivity for the different geometries at normal incidence for a single facet, TE polarization (left), and in the presence of its neighbor (center: TE; right: TM) as a function of θ_{facet}. Values are normalized to the reflection from an isolated perfect-metal facet.

The reflectivity was measured by sending a Gaussian beam, wavelength centered on 1.55 μm, aimed at the center of the facet and incident at an angle θ_{facet} and measuring the reflected field, integrated over time, close above the facet. The far field was determined from this detector for a wavelength of 1.55 μm and the value at the expected reflected output angle $-\theta_{\text{facet}}$ extracted. The results are all normalized using the same geometry for a perfect metal reflector. The FDTD simulations were run with a grid spacing of 25 nm for non-metal facets and 20 nm for metal facets, which are determined to be sufficient through standard convergence tests.

In Table 5, the reflectivity of the different geometries is compared at normal incidence $(\theta_{\text{facet}} = 0^\circ)$ for the first four facet types and at $\theta_{\text{facet}} = 30^\circ$ for the oblique-TIR configuration, for a single facet alone and with a neighbor. When considering the single facet, the best performance is obtained with the metal followed by the DBR and the TIR (99.8%, 99.4%, and 97.3%, respectively) in TE polarization and DBR, metallized and TIR in TM (97.2%, 96.3%, and 95%). The normal incidence results are comparable for the majority of facets, as would be expected from normal incidence. The discrepancy in the metallized facet may be due to a polarization-dependent plasmonic loss.

The addition of the neighboring facet causes a reduction in the reflectivity for most facet types. The TE polarization suffers heavier scattering losses, as reported, for instance, in [8]. The presence of a neighbor does not affect the performance in the case of the corner mirror for both polarizations, and in the case of the simple etch for TM. The high reflectivity obtained with the oblique-TIR with a neighbor is due to the relatively small step size associated with this θ_B leading to much reduced shadowing.

One can see in Fig. 23 the evolution of reflection with θ_{facet} for the single facet (TE only) and for the facet in the presence of a neighbor (TE and TM). The metal facet offers the broadest angular tolerance for a single facet, but its performance in the presence of a neighbor is limited by attenuation and further decreased as the angle increases due to shadowing. For a single facet, the DBR maintains reflectivity above 95% between $\pm 10^\circ$; within that range, it is also the best design when accounting for the neighboring facet in both polarizations.

The behavior of the simple etching facet follows the expected Fresnel reflection behavior with the addition of shadowing when including a neighboring facet. The DBR and metallized facets are closer in performance in the TM simulations with a neighbor facet with the DBR again showing

better performance at small angles. At intermediate angles, the metallized facets tend to perform best in both polarizations.

The corner mirror offers the worst performance as θ_{facet} increases, even for small angles. The corner mirror always reflects the intensity back in the direction of incidence, causing the intensity at the expected reflected angle to follow that of a diffraction pattern from a single facet, hence the sinc function like response with angle. This would effectively make any blazing of a grating with corner mirrors ineffective as they will always blaze themselves back toward the input. As such, to get the best performance from a corner mirror, one would need to make the facets small, thus creating a wide diffracted beam, while balancing against the loss introduced by the additional scattering from the increase in the number of corners.

From this, one can see that a DBR with well-defined vertical facets provides the best overall performance for small angles of θ_{facet}, followed by the metallized surface in both polarization states. The performance of a DBR will also depend strongly on material and quality of fabrication, and in low-index-contrast materials, the bandwidth may be too low for them to be effective. For example, in non-absorbing dielectric materials, the bandwidth at normal incidence is given by [28]

$$\Delta\lambda_{\text{DBR}} \approx \frac{\lambda(n_1 - n_2)}{(n_1 + n_2)}$$

where $\Delta\lambda_{\text{DBR}}$ is the bandwidth of a DBR, and n_1 and n_2 are the effective refractive indices in the repeating sections making up the DBR.

This all leads to the definition of another rule.

Rule 10: Use DBR for small angles (e.g., $\theta_{\text{facet}} < 10^\circ$ in Si) in materials with a sufficiently high index contrast, metallized facets for intermediate angles (e.g., $10^\circ < \theta_{\text{facet}} < \theta_c$) or low-index-contrast materials, and oblique TIR for large angles of incidence $(\theta_{\text{facet}} > \theta_c)$.

5. Conclusion

In this paper, we have presented a new EG design, which we term the PCG, defined on the Rowland mount with facet positions adjusted to maintain phase coherence of the signal while using the focusing properties of this curvature of the grating line. This device has been shown to be a great improvement over the standard Rowland grating, where a like-for-like comparison has been demonstrated. In this paper, the PCG was limited to a grating line based on the Rowland grating mount. The waveguides were also terminated on the RC. Despite these two limitations, a device comparable to the TSPG was defined. Further investigation into other grating lines and waveguide array positions are now possible using this methodology, with the possibility of further improvement.

A detailed analysis of the design of echelle-based WDM devices was presented, which is backed up by simulation. From this analysis, a series of general design rules has been presented that will guide the WDM designer.

These guidelines and rules have been applied where applicable to two designs based around the TSPG and the PCG and, through simulation, their relative performances compared. In both designs, a grating with a theoretical low average insertion loss of -1.9 dB and crosstalk as low as -55 dB between neighboring channels in single-mode operation has been demonstrated. In the authors' belief, the TSPG is the highest performing existing echelle WDM design, and the new PCG design has been shown to provide comparable performance, with PCG showing slightly better channel uniformity and TPSG showing slightly better worst-case crosstalk.

References

[1] M. K. Smit and C. Dam, "PHASAR-based WDM-devices: Principles, design and applications," *IEEE J. Sel. Topics Quantum Electron.*, vol. 2, no. 2, pp. 236–250, Jun. 1996.

[2] H. Takahashi, S. Suzuki, K. Kato, and I. Nishi, "Arrayed waveguide grating for wavelength division multi/demultiplexer with nanometer resolution," *Electron. Lett.*, vol. 26, no. 2, pp. 87–88, Jan. 1990.

[3] N. Ismail, F. Sun, G. Sengo, K. Wörhoff, A. Driessen, R. De Ridder, and M. Pollnau, "Improved arrayed-waveguide-grating layout avoiding systematic phase errors," *Opt. Exp.*, vol. 19, no. 9, pp. 8781–8794, Apr. 2011.
[4] D. Feng, W. Qian, H. Liang, C. Kung, J. Fong, B. Luff, and M. Asghari, "Fabrication insensitive echelle grating in silicon-on-insulator platform," *IEEE Photon. Technol. Lett.*, vol. 23, no. 5, pp. 284–286, Mar. 2010.
[5] J. Brouckaert, W. Bogaerts, S. Selvaraja, P. Dumon, R. Baets, and D. Van Thourhout, "Planar concave grating demultiplexer with high reflective Bragg reflector facets," *IEEE Photon. Technol. Lett.*, vol. 20, no. 4, pp. 309–311, Feb. 2008.
[6] V. I. Tolstikhin, A. Densmore, K. Pimenov, Y. Logvin, F. Wu, S. Laframboise, and S. Grabtchak, "Monolithically integrated optical channel monitor for DWDM transmission systems," *J. Lightwave Technol.*, vol. 22, no. 1, pp. 146–153, Jan. 2004.
[7] W. Bogaerts, S. Selvaraja, P. Dumon, J. Brouckaert, K. De Vos, D. Van Thourhout, and R. Baets, "Silicon-on-insulator spectral filters fabricated with CMOS technology," *IEEE J. Sel. Topics Quantum Electron.*, vol. 16, no. 1, pp. 33–44, Jan./Feb. 2010.
[8] A. Delâge, S. Bidnyk, P. Cheben, K. Dossou, S. Janz, B. Lamontagne, M. Packirisamy, and D. Xu, "Recent developments in integrated spectrometers," in *Proc. 6th Int. Conf. Transp. Opt. Netw.*, 2004, vol. 2, pp. 78–83.
[9] F. Horst, W. Green, B. Offrein, and Y. Vlasov, "Silicon-on-insulator echelle grating WDM demultiplexers with two stigmatic points," *IEEE Photon. Technol. Lett.*, vol. 21, no. 23, pp. 1743–1745, Dec. 2009.
[10] M. Packirisamy and A. Delâge, "Planar waveguide echelle grating device with astigmatic grating facets," U.S. Patent 6 766 077, Jul. 20, 2004.
[11] M. Born and E. Wolf, *Principles of Optics*, 7th ed. Cambridge, U.K.: Cambridge Univ. Press, 1999.
[12] W. Press, S. Teukolsky, W. Vetterling, and B. Flannery, *Numerical Recipes in C*. Cambridge, U.K.: Cambridge Univ. Press, 2002, pp. 402–405.
[13] *EpipProp*, ver. V1.2.0, Photon Design Ltd., Oxford, U.K., Oct. 8, 2012.
[14] S. Bidnyk, A. Balakrishnan, A. Delâge, M. Gao, P. A. Krug, P. Muthukumaran, and M. Pearson, "Planar comb filters based on aberration-free elliptical grating facets," *J. Lightwave Technol.*, vol. 23, no. 3, pp. 1239–1243, Mar. 2005.
[15] F. Horst, W. Green, B. Offrein, and Y. Vlasov, "Echelle grating WDM (de-) multiplexers in SOI technology, based on a design with two stigmatic points," in *Proc. of SPIE*, 2008, pp. 69960R-1–69960R-8.
[16] P. Cheben, "Wavelength dispersive planar waveguide devices: Echelle and arrayed waveguide gratings," in *Optical Waveguides: From Theory to Applied Mechanics*. Boca Raton, FL, USA: CRC Press, 2007.
[17] D. Feng, N. Feng, C. Kung, H. Liang, W. Qian, J. Fong, B. Luff, and M. Asghari, "Compact single-chip VMUX/DEMUX on the silicon-on-insulator platform," *Opt. Exp.*, vol. 19, no. 7, pp. 6125–6130, Mar. 2011.
[18] J.-J. He, E. S. Koteles, B. Lamontagne, L. Erickson, A. Delâge, and M. Davies, "Integrated polarization compensator for WDM waveguide demultiplexers," *IEEE Photon. Technol. Lett.*, vol. 11, no. 2, pp. 224–226, Feb. 1999.
[19] P. Cheben, D.-X. Xu, S. Janz, A. Delage, and D. Dalacu, "Birefringence compensation in silicon-on-insulator planar waveguide demultiplexers using a buried oxide layer," in *Proc. SPIE*, Jun. 2003, vol. 4997, pp. 181–189.
[20] *FIMMWAVE with FIMMPROP*, ver. V5.4.1, Photon Design Ltd., Oxford, U.K., Aug. 26, 2012.
[21] L. B. Soldano and E. Pennings, "Optical multi-mode interference devices based on self-imaging: Principles and applications," *J. Lightwave Technol.*, vol. 13, no. 4, pp. 615–627, Apr. 1995.
[22] J. B. D. Soole, M. R. Amersfoort, H. P. LeBlanc, N. C. Andreadakis, A. Rajhel, C. Caneau, R. Bhat, M. A. Koza, C. Youtsey, and I. Adesida, "Use of multimode interference couplers to broaden the passband of wavelength-dispersive integrated WDM filters," *IEEE Photon. Technol. Lett.*, vol. 8, no. 10, pp. 1340–1342, Oct. 1996.
[23] Y. Doi, M. Ishii, S. Kamei, S. Ogawa, S. Mino, T. Shibata, Y. Hida, T. Kitagawa, and K. Kato, "Flat and high responsivity CWDM photoreceiver using silica-based AWG with multimode output waveguides," *Electron. Lett.*, vol. 39, no. 22, pp. 1603–1604, Oct. 2003.
[24] J.-J. He, B. Lamontagne, L. Erickson, M. Davies, and E. Koteles, "Monolithic integrated wavelength demultiplexer based on a waveguide Rowland circle grating in InGaAsP/InP," *J. Lightwave Technol.*, vol. 16, no. 4, pp. 631–638, Apr. 1998.
[25] J.-J. He, "Phase-dithered waveguide grating with flat passband and sharp transitions," *IEEE J. Sel. Topics Quantum. Electron.*, vol. 8, no. 6, pp. 1186–1193, Nov./Dec. 2002.
[26] Z. Shi, J. He, and S. He, "An analytic method for designing passband flattened DWDM demultiplexers using spatial phase modulation," *J. Lightwave Technol.*, vol. 21, no. 10, pp. 2314–2321, Oct. 2003.
[27] *OmniSim*, ver. V4.8.2 (x64), Photon Design, Ltd., Oxford, U.K., Nov. 30, 2012.
[28] J. Buus, M. Amann, and D. Blumenthal, *Tunable Laser Diodes and Related Optical Sources*, 2nd ed. Hoboken, NJ, USA: Wiley, 2005, p. 52.